

Tunable Semiconductors: Control over Carrier States and Excitations in Layered Hybrid Organic-Inorganic Perovskites

Chi Liu,¹ William Huhn,² Ke-Zhao Du,² Alvaro Vazquez-Mayagoitia,³ David Dirkes,⁴ Wei You,⁴ Yosuke Kanai,⁴ David B. Mitzi,^{2,1} and Volker Blum^{2,1}

¹*Department of Chemistry, Duke University, Durham, North Carolina 27708, USA*

²*Department of Mechanical Engineering and Materials Science, Duke University, Durham, North Carolina 27708, USA*

³*Argonne Leadership Computing Facility, 9700 S. Cass Avenue, Lemont IL 60439, USA*

⁴*Department of Chemistry, University of North Carolina, Chapel Hill, North Carolina 27599, USA*

(Dated: March 9, 2024)

For a class of 2D hybrid organic-inorganic perovskite semiconductors based on π -conjugated organic cations, we predict quantitatively how varying the organic and inorganic component allows control over the nature, energy and localization of carrier states in a quantum-well-like fashion. Our first-principles predictions, based on large-scale hybrid density-functional theory with spin-orbit coupling, show that the interface between the organic and inorganic parts within a single hybrid can be modulated systematically, enabling us to select between different type-I and type-II energy level alignments. Energy levels, recombination properties and transport behavior of electrons and holes thus become tunable by choosing specific organic functionalizations and juxtaposing them with suitable inorganic components.

Hybrid organic-inorganic perovskites (HOIPs), [1, 2] particularly three-dimensional (3D) HOIPs, are currently experiencing a strong revival in interest as economically processable, optically active semiconductor materials with excellent transport characteristics. Their success is showcased most prominently by record performance gains in proof-of-concept photovoltaic [3–12] and light-emitting devices. [13–20] The electronic function of 3D HOIPs can be tuned to a limited extent by manipulating the inorganic component (from which the frontier orbitals are derived), but the organic cations are confined by the 3D structure and are thus necessarily small (e.g., methylammonium [3–8, 13–18] and formamidinium [9–11, 19, 21, 22]), with electronic levels that do not contribute directly to the electronic functionality. [23–28] However, the accessible chemical space of HOIPs extends well beyond the 3D systems. [1] In particular, the layered, so-called two-dimensional (2D) perovskites do not place a strict length constraint on the organic cation. In these materials, a much broader range of functional organic molecules can be incorporated within the inorganic scaffolds, including complex functional molecules such as oligo-acene or -thiophene derivatives. [1, 29–37] Fig. 1a shows the atomic structure of a paradigmatic example of such a 2D HOIP with active organic functionality, bis(aminoethyl)-quaterthiophene lead bromide AE4TPbBr₄. [34] Similar juxtapositions of targeted organic and inorganic components give rise to a vast, yet systematically accessible space of possible semiconductor materials, [1, 2, 38–40] including those in which the molecular carrier levels contribute directly to the low-lying excitations and carrier levels. [1, 30–32, 34, 38, 39, 41] This large space of conceivable organic-inorganic combinations thus offers the unique opportunity to tailor (ideally with computational guidance) materials with particularly desirable semiconductor properties, by intentionally controlling the spatial location and character of the

electronic carriers and optical excitations throughout the material.

A key physical prerequisite to manipulate the semiconductor properties of layered hybrid materials is to understand the nature and spatial localization of their carriers and excitations. Specifically, the question of whether and how exactly one can understand their properties in analogy to quantum wells with varying confinement barriers (often assumed [40, 42–44]) is subject to discussion in the literature. [45–48] Fig. 1b exemplifies the principle by comparing four different, conceivable quantum-well like situations: “Type I”, with low-energy electrons and holes localized on the same component (either organic, Ia or inorganic, Ib) or “Type II”, with electrons and holes on different components (holes on inorganic, electrons on organic, IIa, or vice versa, IIb). While some simple layered HOIPs have been successfully explained in a type-Ib picture (inorganic band edges with the organic acting as a quasi-inert screening medium [40, 42–44, 46–48]), a fully quantitative understanding of both band gaps within and band alignment between the materials’ components is essential to recover the larger set of possibilities in Fig. 1b. Providing this understanding for the large, complex crystal structures at hand constitutes a substantial challenge for current theory, both regarding computational resources and sufficiently accurate approximations. In this paper, we demonstrate that these challenges can now be met, enabling us to answer questions that are central to future targeted developments of new HOIP semiconductors: (1) Can these structures be understood as quantum-well-like structures with spatially well-separated levels in the organic vs. inorganic components, or will the electronic states be hybridized and thus delocalized across both components? (2) What is the spatial nature of electron/hole carriers within the structure? For instance, do they tend to migrate to the organic or the inorganic hybrid component in the lowest-

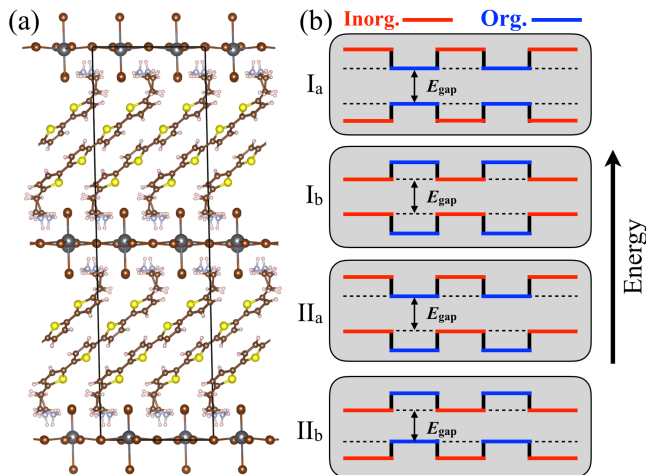


FIG. 1. Structure of AE4TPbBr₄ fully relaxed by DFT-PBE+TS taking the experimental (X-ray diffraction) structure[34] as the input. Possible energy level schemes (Ia, Ib, IIa, IIb) for the alternating organic-inorganic perovskite structure are shown, with the overall band gap indicated by arrows and dashed lines.

energy configuration, drastically affecting each carrier’s transport properties (band-like inorganic vs. hopping-like organic)? (3) To what extent can we rationally tune the carrier and excitation properties by independently varying the organic and inorganic components?

Whether we can uncover a new paradigm using 2D HOIPs as “semiconductors on demand” with finely tunable properties and high-precision crystalline structural control depends on building a design principle that relates complex hybrid atomic structures to optoelectronic properties through answering the questions above. In this work, we do so through a first-principles theoretical examination of a class of oligothiophene-based 2D HOIPs, expanding on the AE4TPbBr₄ compound shown in Fig.1a. A practical challenge for theory is the structural complexity of these 2D HOIPs for which the unit cells are large. For instance, a (2×2) lateral supercell of the perovskite layer (Figures S1, S2, S3 in the Supplemental Material (SM) [49]) in this and other structures considered in this work is needed to cover the experimentally correct perovskite layer distortion and molecular arrangement, leading to 424 atoms in the simulation cell for AE4TPbBr₄. The (2×2) supercell instead of the experimentally reported (1×2) structure is necessary with regards to both accessing an energetically lower structure (Table S1 [49]) and also removing the disordering in the inorganic and organic structural components in the experimental structure. In addition, the two inorganic layers in the (1×2) relaxed structure have different Pb-Br-Pb angles, which disagrees with the experimental structure of AE4TPbBr₄ (Fig. S4 [49]). For structure predictions that capture the subtle balance of different molecular and inorganic bonding contributions, we use van der Waals corrected semilocal density-functional theory

(DFT—i.e., Perdew-Burke-Ernzerhof (PBE) exchange-correlation functional,[55] plus the Tkatchenko-Scheffler (TS) pairwise dispersion scheme[56]). Electronic properties require a higher level of theory for qualitatively correct results, but the most attractive first-principles many-body approaches such as the *GW* approximation[57, 58] remain out of reach for structures of this size. For band structure predictions, we therefore resort to the still demanding level of hybrid DFT using the Heyd-Scuseria-Ernzerhof (HSE06) functional[59, 60]) including spin-orbit coupling (SOC)[61]. Importantly, and unlike semilocal DFT, hybrid DFT in principle contains the right physics[62] to capture the frontier energy levels (valence band maximum (VBM) and conduction band minimum (CBM)). Including SOC is critical to capture correctly the qualitative underlying nature of carriers, changing the nature of the CBM from “organic” to “inorganic” in AE4TPbBr₄ and reducing the band gap by ~ 0.3 eV (Fig. S5 [49]).

All calculations are performed by the FHI-aims code,[57, 61, 63–67] using the ELSI infrastructure[68] and ELPA eigenvalue solver[69] for massively parallel simulations. For all crystal geometries, we employ full relaxation of unit cell parameters and cell-internal atomic coordinates[70] using the FHI-aims “tight” numerical defaults (Table S2 [49]) and k-point grids settings of 1×2×2 (Table S3 [49]). For band structures, FHI-aims’ “intermediate” settings (Table S4 [49]) and dense k-point grids of 3×3×3 are used. The exchange mixing parameter in HSE06 was kept at 25% and the screening parameter at $\Omega = 0.11 \text{ Bohr}^{-1}$ [71] in order to retain a single consistent base to compare energy band structures across different materials in this work. We first validate this approach for the low-temperature orthorhombic phase of MAPbI₃ (Fig. S6a [49]). The lattice parameters predicted by DFT-PBE+TS agree with the experimental values [72] to within 1.4% (Fig. S6b [49]). The HSE06+SOC approach predicts a direct band gap of 1.42 eV, which underestimates the experimental value (1.65-1.68 eV, Fig. S6b [49]) by 0.2-0.3 eV.[73, 74]. Details of how we constructed the computational models for all structures considered in this work can be found in the SM, section IX.[49] For AE4TPbBr₄ (Fig. 1a), deviations of any unit cell parameters of the resulting predicted structure compared to experiment are 1.2% or better, i.e., they are in excellent agreement (Table S5 [49]). Finally, a new crystalline sample of AE4TPbI₄ was grown and an X-ray structure refinement performed (SM section X [49]), also indicating excellent agreement with the DFT-predicted structure used in the analyses below (Table S5 [49]).

Turning first to energy level localization, orbital plots (see Figures S9, S10, S11 [49] for example orbitals of AE4TPbX₄, X = Cl, Br, I) show that the states associated with inorganic and organic components are spatially well-separated, supporting the notion of “quantum-well like” states in these materials. This answers question (1) above and validates a discussion in terms of separate “inorganic” and “organic” bands. Even *et al.*[47, 48] have

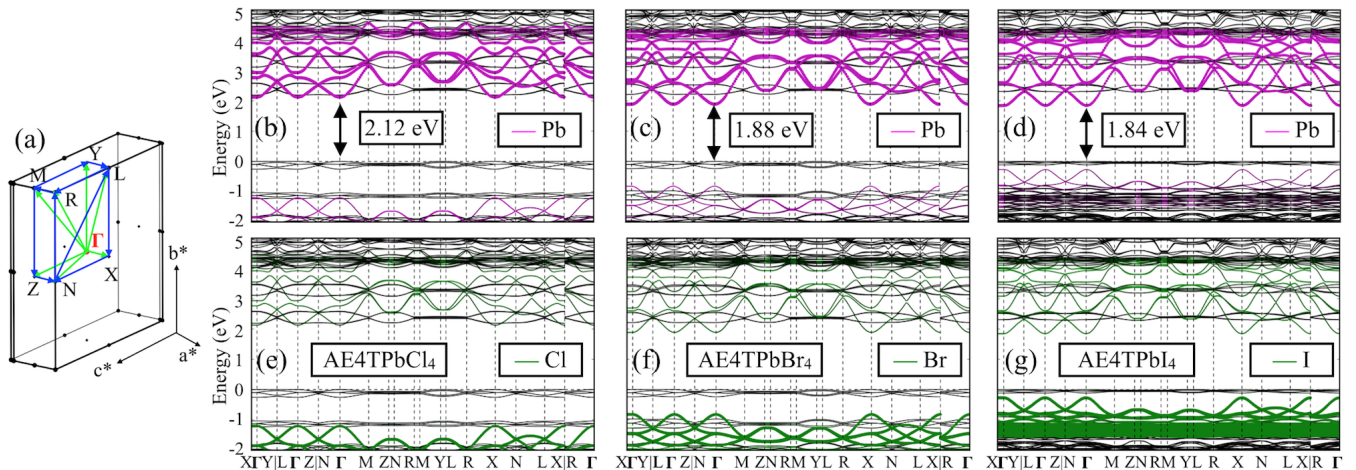


FIG. 2. Band structures of AE4TPbX_4 ($X = \text{Cl}, \text{Br}, \text{I}$) calculated by DFT-HSE06+SOC with the states of Pb (b-d) and halogen (e-g) identified by projected density of states onto different species. The K path in the reciprocal space is shown in subfigure (a). The energy zero in (b-g) is set equal to the valence band maximum (for internal alignments relative to Pb $1s$ levels, see Figure 3a below).

also considered 2D HOIPs from the perspective of semiconductor quantum wells, showing that the effective mass model may fail due to the absence of superlattice coupling and importance of non-parabolicity. They proposed a computational analysis in terms of separate, neutralized organic and inorganic layers, appropriate for type-Ib situations. In the current work, we cover the full set of materials directly, allowing us to assess band gaps within each component as well as the alignments of their electronic levels. Knowing the alignments enables us to assess the full space of possible HOIP semiconductors (e.g., type-I and II), where both the inorganic and the organic components are electronically active.

The halogen atoms in the inorganic framework offer a convenient handle for tailoring the associated electronic structure of the inorganic component by varying it from Br to Cl and I.[34] Full band structures for the compound series AE4TPbX_4 ($X = \text{Cl}, \text{Br}, \text{I}$) are shown in Fig. 2. All three compounds have a direct band gap at the Γ point. By changing the halogen, the dispersive bands originating from the inorganic component (Pb- and halogen-derived states, colored lines in Figures 2b-g) shift substantially with respect to the organic bands. In contrast, the organic-derived bands (black lines in Figures 2b-g) vary only slightly among these three compounds. Full and partial densities of states for these and other compounds in Figures S14-S15 [49] corroborate the chemical makeup shown in the band structures. Band curvature parameters (Table S6) that correspond to the diagonal elements of the effective mass tensors[75–77] in the reciprocal-space coordinate system of Fig. 2a confirm some qualitative trends emerging from the band structures: Uniformly flat bands (effective masses $>20 m_e$) perpendicular to the perovskite planes indicate hindered, non-bandlike transport. Somewhat lower effective mass

tensor elements ($2.2\text{--}11.4 m_e$, still higher than in typical semiconductor materials) emerge for the holes (VBM) on the organic components parallel to the planes. Low effective mass tensor elements, $\approx 0.2\text{--}0.5 m_e$, for the electrons (CBM) along the inorganic planes, in the range typical of 3D perovskites[76, 77] might, absent other detrimental factors, indicate relatively easy electron transport.

The trends of the “organic” and “inorganic” frontier energy levels are shown in Figure 3a. The average of Pb $1s$ energy levels is chosen to formally align energy levels between different HOIPs in Fig. 3. However, we did not study how this choice (equivalent to the absence of dipolar fields between Pb ions across an interface between two different HOIPs) pertains to real interfaces between HOIPs and the conclusions of this work do not rely on this convention. Replacing Br by Cl increases the overall computed band gap from 1.88 eV to 2.12 eV, whereas the substitution by I decreases the energy gap value to 1.84 eV. While the *inorganic* energy gap changes drastically from 2.70 to 3.32/2.11 eV for Cl/I substitutions (Fig. 3), the associated change in the *organic* energy gap is negligibly small (~ 0.1 eV). However, a drastic change evident from both Figures 2 and 3a is the ordering of the levels, particularly the electron-like (CBM) states when going from Cl to Br and I. For Br and I, the band structures indicate Type IIb (Fig. 1) like quantum well behavior, i.e., electrons and holes are expected to be spatially well separated on the inorganic and organic components, respectively. In contrast, the organic and inorganic CBM levels are predicted to lie within a few tens of meV for the Cl-substituted compounds, i.e., they are essentially degenerate within the uncertainties of the HSE06+SOC treatment employed here. AE4TPbCl_4 is thus between types Ia and IIb in Fig. 1b and would allow electrons to travel to either component with reasonable ease at finite

temperature. This difference would have profound implications for the expected carrier recombination properties of all three compounds, as evidenced, e.g., in photoluminescence (PL). In fact, strong quaterthiophene PL emission at ~ 540 nm (2.30 eV) was experimentally observed for $X = \text{Cl}$, [34] whereas the analogous PL features are substantially quenched for $X = \text{Br}, \text{I}$. Our present computational result agrees with and explains this experimental observation. While the $X = \text{Cl}$ compound displays a near type-Ia band alignment, the $X = \text{Br}, \text{I}$ compounds are clearly type-IIb. In the latter two compounds, the energy level alignment therefore effectively impedes the electron-hole recombination since the electrons and the holes are preferentially located across the interface in the inorganic and organic hybrid components, respectively, i.e., addressing question (2) from the introduction.

The importance of a fully predictive, quantitative theoretical treatment is further underscored by the fact that a discussion based on qualitative factors in 1999 led to the different conclusion of type-IIa, not type-IIb alignment for this compound. [34] We note that optical excitations in absorption or emission cannot be expected to be captured based on the band structures derived in this work alone, since the typically strong excitonic effects are not included. For instance, exciton binding energies up to 540 meV have been reported on the inorganic compound in 2D perovskites [1, 78] and an exciton binding energy of 0.4 eV has been reported in organic (not hybrid) sexithiophene thin films. [79] However, the qualitative localization of carriers prior to recombination (discussed above) still provides valuable insights into their expected recombination properties. We also note that the potential implications of being able to tune levels on the organic and inorganic components independently reach beyond optical properties alone, affecting (for example) transport properties, dopability, or band offsets (and thus potential energy losses in devices) between the components.

We finally consider the ability to tune the band gap and quantum well nature of the structure by varying the organic component, changing the conjugation length of the oligothiophene molecules. As shown in Fig. 3b, we substitute the “all-anti” configuration (successive S atoms on alternating sides) of bis-ethylamine terminated oligothiophene AEnT ($n = 1, 2, 3, 4, 5$, Fig. 3c) into the scaffold of AE4TPbBr₄. While the quaterthiophene molecule in experimental AE4TPbBr₄ (Fig. 1) adopts a syn-anti-syn configuration [34], this configuration cannot be adopted by all AEnT ($n = 1, 2, 3, 4, 5$) oligothiophenes. For the purpose of having a systematic assessment, we thus restrict this part of our study to the all-anti configuration. Note, however, that the predicted electronic properties are only expected to be insignificantly affected by this conformational change as shown by the additional symbols corresponding to the syn-anti-syn conformation for $n=4$ (Fig. 3b). The electronic band structures reveal direct gaps for all considered conjugation lengths of AEnTPbBr₄ (Fig. S12 [49]) and band curvature trends (Table S7) are broadly consistent with those discussed for

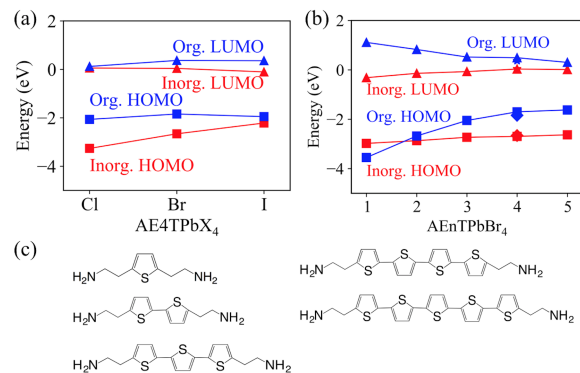


FIG. 3. (a) Frontier energy levels of the organic and inorganic components at the Γ point among the series of AE4TPbX₄ ($X = \text{Cl}, \text{Br}, \text{I}$). (b) Frontier energy levels at the Γ point among the series of AEnTPbBr₄ ($n = 1, 2, 3, 4, 5$). Stars and diamonds indicate the energy levels of syn-anti-syn AE4TPbBr₄ for $n = 4$. The average of Pb 1s energies is chosen to align the energy levels of different compounds. (c) Oligothiophene-based organic molecules considered in the all-anti configuration for varying the number n .

AE4TPbX₄ above. The overall band gap decreases as n increases, i.e., 2.66, 2.54, 1.98, 1.73 and 1.63 for $n = 1, 2, 3, 4, 5$, respectively. The predicted AEnTPbBr₄ compounds for $n = 2-5$ yield type-IIb level alignments. However, the $n = 1$ compound reveals a type-Ib alignment (both CBM and VBM derived from the inorganic component). This behavior (type Ib) is consistent with other 2D perovskites with smaller organic functionality, in which carriers/excitons are mainly funneled onto the inorganic subcomponent. [46–48, 80] We thus affirmatively answer question (3) above – i.e., the carrier nature and neutral excitation properties and overall gap can be varied rationally by changing the organic component or the inorganic component in 2D HOIPs independently.

In summary, our results show that the quantum-well model can be used for conceptual understanding and as a useful starting point as a design principle for the layered HOIP family of hybrid materials. The tunability of electronic properties, exemplified by the materials studied in this work, opens up the possibility to computationally predict and tailor nanoscale charge separation or recombination, as well as spatially separated charge transport within the much larger overall class of hybrid crystalline materials. Clearly, significant challenges would remain if theory were applied in isolation. For example, capturing all structural subtleties of complex 2D HOIP arrangements is nontrivial, as is predicting fundamental gaps with an accuracy of better than a few tenths of an eV (the accuracy expected from the unmodified HSE06+SOC functional [71], as used in this work, for typical semiconductors [75, 81, 82]) for structures of this size. Excitingly, the combination of such predictions with subsequent targeted experimental syntheses overcomes these challenges, creating enormous possibilities to iden-

tify and fine-tune entirely new layered crystalline organic-inorganic semiconductors with deliberately selected optoelectronic/electronic properties.

ACKNOWLEDGMENTS

This work was financially supported by the NSF under awards number DMR-1729297 and DMR-1728921, as

well as through the Research Triangle MRSEC (DMR-11-21107). An award of computer time was provided by the Innovative and Novel Computational Impact on Theory and Experiment (INCITE) program, and the Theta Early Science program (ESP). This research used resources of the Argonne Leadership Computing Facility (ALCF), which is a DOE Office of Science User Facility supported under Contract DE-AC02-06CH11357.

-
- [1] B. Saparov and D. B. Mitzi, *Chem. Rev.* **116**, 4558 (2016).
- [2] W. Li, Z. Wang, F. Deschler, S. Gao, R. H. Friend, and A. K. Cheetham, *Nat. Rev. Mater.* **2**, 16099 (2017).
- [3] A. Kojima, K. Teshima, Y. Shirai, and T. Miyasaka, *J. Am. Chem. Soc.* **131**, 6050 (2009).
- [4] J. H. Heo, S. H. Im, J. H. Noh, T. N. Mandal, C.-S. Lim, J. A. Chang, Y. H. Lee, H. J. Kim, A. Sarkar, M. K. Nazeeruddin, M. Grätzel, and S. I. Seok, *Nat. Photonics* **7**, 486 (2013).
- [5] D. Liu and T. L. Kelly, *Nat. Photonics* **8**, 133 (2013).
- [6] N. J. Jeon, J. H. Noh, Y. C. Kim, W. S. Yang, S. Ryu, and S. I. Seok, *Nat. Mater.* **13**, 897 (2014).
- [7] M. A. Green, A. Ho-Baillie, and H. J. Snaith, *Nat. Photonics* **8**, 506 (2014).
- [8] P. Gao, M. Grätzel, and M. K. Nazeeruddin, *Energy Environ. Sci.* **7**, 2448 (2014).
- [9] G. E. Eperon, S. D. Stranks, C. Menelaou, M. B. Johnston, L. M. Herz, and H. J. Snaith, *Energy Environ. Sci.* **7**, 982 (2014).
- [10] W. S. Yang, J. H. Noh, N. J. Jeon, Y. C. Kim, S. Ryu, J. Seo, and S. I. Seok, *Science* **348**, 1234 (2015).
- [11] W. S. Yang, B.-W. Park, E. H. Jung, N. J. Jeon, Y. C. Kim, D. U. Lee, S. S. Shin, J. Seo, E. K. Kim, J. H. Noh, and S. I. Seok, *Science* **356**, 1376 (2017).
- [12] A. D. Jodlowski, C. Roldán-Carmona, G. Grancini, M. Salado, M. Ralaiarisoa, S. Ahmad, N. Koch, L. Camacho, G. de Miguel, and M. K. Nazeeruddin, *Nature Energy* **2**, 972 (2017).
- [13] Z.-K. Tan, R. S. Moghaddam, M. L. Lai, P. Docampo, R. Higler, F. Deschler, M. Price, A. Sadhanala, L. M. Pazos, D. Credgington, F. Hanusch, T. Bein, H. J. Snaith, and R. H. Friend, *Nature Nanotechnology* **9**, 687 (2014).
- [14] J. Wang, N. Wang, Y. Jin, J. Si, Z.-K. Tan, H. Du, L. Cheng, X. Dai, S. Bai, H. He, Z. Ye, M. L. Lai, R. H. Friend, and W. Huang, *Advanced Materials* **27**, 2311 (2015).
- [15] Y.-H. Kim, H. Cho, J. H. Heo, T.-S. Kim, N. Myoung, C.-L. Lee, S. H. Im, and T.-W. Lee, *Adv. Mater.* **27**, 1248 (2015).
- [16] H. Cho, S.-H. Jeong, M.-H. Park, Y.-H. Kim, C. Wolf, C.-L. Lee, J. H. Heo, A. Sadhanala, N. Myoung, S. Yoo, S. H. Im, R. H. Friend, and T.-W. Lee, *Science* **350**, 1222 (2015).
- [17] Y.-H. Kim, H. Cho, and T.-W. Lee, *Proc. Natl. Acad. Sci.* **113**, 11694 (2016).
- [18] Z. Xiao, R. A. Kerner, L. Zhao, N. L. Tran, K. M. Lee, T.-W. Koh, G. D. Scholes, and B. P. Rand, *Nat. Photonics* **11**, 108 (2017).
- [19] X. Zhang, H. Liu, W. Wang, J. Zhang, B. Xu, K. L. Karen, Y. Zheng, S. Liu, S. Chen, K. Wang, and X. W. Sun, *Adv. Mater.* **29**, 1606405 (2017).
- [20] S. Adjokatse, H.-H. Fang, and M. A. Loi, *Mater. Today* **20**, 413 (2017).
- [21] D. B. Mitzi and K. Liang, *J. Solid State Chem.* **134**, 376 (1997).
- [22] Q. Han, S.-H. Bae, P. Sun, Y.-T. Hsieh, Y. M. Yang, Y. S. Rim, H. Zhao, Q. Chen, W. Shi, G. Li, and Y. Yang, *Adv. Mater.* **28**, 2253 (2016).
- [23] T. Umebayashi, K. Asai, T. Kondo, and A. Nakao, *Phys. Rev. B* **67**, 155405 (2003).
- [24] F. Chiarella, A. Zappettini, F. Licci, I. Borriello, G. Cantale, D. Ninno, A. Cassinese, and R. Vaglio, *Phys. Rev. B* **77**, 045129 (2008).
- [25] A. Filippetti and A. Mattoni, *Phys. Rev. B* **89**, 125203 (2014).
- [26] F. Brivio, A. B. Walker, and A. Walsh, *APL Mater.* **1**, 042111 (2013).
- [27] F. Brivio, K. T. Butler, A. Walsh, and M. van Schilfgaarde, *Phys. Rev. B* **89**, 155204 (2014).
- [28] C. Motta, F. El-Mellouhi, S. Kais, N. Tabet, F. Alharbi, and S. Sanvito, *Nat. Commun.* **6**, 7026 (2015).
- [29] M. Era, K. Maeda, and T. Tsutsui, *Chem. Phys. Lett.* **296**, 417 (1998).
- [30] M. Braun, W. Tuffentsammer, H. Wachtel, and H. Wolf, *Chem. Phys. Lett.* **303**, 157 (1999).
- [31] Z. Xu and D. B. Mitzi, *Chem. Mater.* **15**, 3632 (2003).
- [32] K. Ema, M. Inomata, Y. Kato, H. Kunugita, and M. Era, *Phys. Rev. Lett.* **100**, 257401 (2008).
- [33] K. Du, Q. Tu, X. Zhang, Q. Han, J. Liu, S. Zauscher, and D. B. Mitzi, *Inorg. Chem.* **56**, 9291 (2017).
- [34] D. B. Mitzi, K. Chondroudis, and C. R. Kagan, *Inorg. Chem.* **38**, 6246 (1999).
- [35] D. B. Mitzi, *Inorg. Chem.* **39**, 6107 (2000).
- [36] X.-H. Zhu, N. Mercier, P. Frère, P. Blanchard, J. Roncali, M. Allain, C. Pasquier, and A. Riou, *Inorg. Chem.* **42**, 5330 (2003).
- [37] M. Era, S. Yoneda, T. Sano, and M. Noto, *Thin Solid Films* **438**, 322 (2003).
- [38] D. B. Mitzi, *Prog. Inorg. Chem.* **48**, 1 (1999).
- [39] D. B. Mitzi, *J. Chem. Soc. Dalton Trans.* **0**, 1 (2001).
- [40] S. Zhang, G. Lanty, J.-S. Lauret, E. Deleporte, P. Audebert, and L. Galmiche, *Acta. Mater.* **57**, 3301 (2009).
- [41] D. Cortecchia, C. Soci, M. Cametti, A. Petrozza, and J. Mart-Rujas, *ChemPlusChem* **82**, 681 (2017).
- [42] T. Ishihara, J. Takahashi, and T. Goto, *Solid State Communications* **69**, 933 (1989).
- [43] M. Era, S. Morimoto, T. Tsutsui, and S. Saito, *Applied Physics Letters* **65**, 676 (1994).
- [44] N. Wang, L. Cheng, R. Ge, S. Zhang, Y. Miao, W. Zou,

- C. Yi, Y. Sun, Y. Cao, R. Yang, Y. Wei, Q. Guo, Y. Ke, M. Yu, Y. Jin, Y. Liu, Q. Ding, D. Di, L. Yang, G. Xing, H. Tian, C. Jin, F. Gao, R. H. Friend, J. Wang, and W. Huang, *Nat. Photonics* **10**, 699 (2016).
- [45] D. B. Mitzi, K. Chondroudis, and C. R. Kagan, *IBM J. Res. Dev.* **45**, 29 (2001).
- [46] E. A. Muljarov, S. G. Tikhodeev, N. A. Gippius, and T. Ishihara, *Phys. Rev. B* **51**, 14370 (1995).
- [47] J. Even, L. Pedesseau, and C. Katan, *ChemPhysChem* **15**, 3733 (2014).
- [48] J. Even, L. Pedesseau, C. Katan, M. Kepenekian, J.-S. Lauret, D. Saponi, and E. Deleporte, *J. Phys. Chem. C* **119**, 10161 (2015).
- [49] See Supplemental Material for: structural details of the perovskites in our simulations; energetic impact of the supercell choice; impact of spin-orbit coupling in the reported energy band structures; computational details (basis sets and k-space grid convergence); validation of computational protocols by comparing to experimental results for MAPbI₃, for AE4TPbBr₄ and for AE4TPbI₄; experimental details for the synthesis and characterization of a new AE4TPbI₄ crystal; and additional computed orbitals, energy band structures, band curvature parameters, full and partial densities of states supporting the general findings demonstrated in the actual paper. Computational validation for MAPbI₃ also includes comparison to a more sophisticated many-body dispersion treatment.[50] Synthesis details include Refs. [51–53]. All computational input and output files (raw data) are available at the NOMAD repository.[54]
- [50] A. Ambrosetti, A. M. Reilly, R. A. DiStasio Jr., and A. Tkatchenko, *J. Chem. Phys.* **140**, 18A508 (2014).
- [51] H. Muguruma, T. Saito, A. Hiratsuka, I. Karube, and S. Hotta, *Langmuir* **12**, 5451 (1996).
- [52] H. Muguruma, T. Saito, S. Sasaki, S. Hotta, and I. Karube, *J. Heterocyclic Chem.* **33**, 173 (1996).
- [53] H. Muguruma, K. Kobiro, and S. Hotta, *Chem. Mater.* **10**, 1459 (1998).
- [54] NOMAD Repository. <http://doi.org/10.17172/NOMAD/2018.09.21-1> (accessed Sep 22, 2018).
- [55] J. P. Perdew, K. Burke, and M. Ernzerhof, *Phys. Rev. Lett.* **77**, 3865 (1996).
- [56] A. Tkatchenko and M. Scheffler, *Phys. Rev. Lett.* **102**, 073005 (2009).
- [57] X. Ren, P. Rinke, V. Blum, J. Wieferink, A. Tkatchenko, A. Sanfilippo, K. Reuter, and M. Scheffler, *New J. Phys.* **14**, 053020 (2012).
- [58] L. Reining, *WIREs Comput. Mol. Sci.* **12**, 1344 (2017).
- [59] J. Heyd, G. E. Scuseria, and M. Ernzerhof, *J. Chem. Phys.* **118**, 8207 (2003).
- [60] J. Heyd, G. E. Scuseria, and M. Ernzerhof, *J. Chem. Phys.* **124**, 219906 (2006).
- [61] W. P. Huhn and V. Blum, *Phys. Rev. Materials* **1**, 033803 (2017).
- [62] J. P. Perdew, W. Yang, K. Burke, Z. Yang, E. K. U. Gross, M. Scheffler, G. E. Scuseria, T. M. Henderson, I. Y. Zhang, A. Ruzsinszky, H. Peng, J. Sun, E. Trushin, and A. Görling, *Proc. Natl. Acad. Sci.* **114**, 2801 (2017).
- [63] V. Blum, R. Gehrke, F. Hanke, P. Havu, V. Havu, X. Ren, K. Reuter, and M. Scheffler, *Comput. Phys. Commun.* **180**, 2175 (2009).
- [64] V. Havu, V. Blum, P. Havu, and M. Scheffler, *J. Comput. Phys.* **228**, 8367 (2009).
- [65] S. V. Levchenko, X. Ren, J. Wieferink, R. Johanni, P. Rinke, V. Blum, and M. Scheffler, *Comput. Phys. Commun.* **192**, 60 (2015).
- [66] I. Y. Zhang, X. Ren, P. Rinke, V. Blum, and M. Scheffler, *New J. Phys.* **15**, 123033 (2013).
- [67] A. C. Ihrig, J. Wieferink, I. Y. Zhang, M. Ropo, X. Ren, P. Rinke, M. Scheffler, and V. Blum, *New Journal of Physics* **17**, 093020 (2015).
- [68] V. W. Yu, F. Corsetti, A. Garca, W. P. Huhn, M. Jacquelin, W. Jia, B. Lange, L. Lin, J. Lu, W. Mi, A. Seifitokaldani, A. Vazquez-Mayagoitia, C. Yang, H. Yang, and V. Blum, *Comput. Phys. Commun.* **222**, 267 (2018).
- [69] A. Marek, V. Blum, R. Johanni, V. Havu, B. Lang, T. Auckenthaler, A. Heinecke, H.-J. Bungartz, and H. Lederer, *J. Phys. Condens. Matter* **26**, 213201 (2014).
- [70] F. Knuth, C. Carbogno, V. Atalla, V. Blum, and M. Scheffler, *Comput. Phys. Commun.* **190**, 33 (2015).
- [71] A. V. Krukau, O. A. Vydrov, A. F. Izmaylov, and G. E. Scuseria, *J. Chem. Phys.* **125**, 224106 (2006).
- [72] M. T. Weller, O. J. Weber, P. F. Henry, A. M. Di Pumpo, and T. C. Hansen, *Chem. Commun.* **51**, 4180 (2015).
- [73] W. Kong, Z. Ye, Z. Qi, B. Zhang, M. Wang, A. Rahimi-Iman, and H. Wu, *Phys. Chem. Chem. Phys.* **17**, 16405 (2015).
- [74] L. Q. Phuong, Y. Yamada, M. Nagai, N. Maruyama, A. Wakamiya, and Y. Kanemitsu, *J. Phys. Chem. Lett.* **7**, 2316 (2016).
- [75] T. Zhu, W. P. Huhn, G. C. Wessler, D. Shin, B. Saparov, D. B. Mitzi, and V. Blum, *Chem. Mater.* **29**, 7868 (2017).
- [76] N. Ashari-Astani, S. Meloni, A. H. Salavati, G. Palermo, M. Grätzel, and U. Roethlisberger, *The Journal of Physical Chemistry C* **121**, 23886 (2017).
- [77] J. Feng and B. Xiao, *The Journal of Physical Chemistry Letters* **5**, 1278 (2014).
- [78] D. B. Straus and C. R. Kagan, *J. Phys. Chem. Lett.* **9**, 1434 (2018).
- [79] I. Hill, A. Kahn, Z. Soos, and R. Pascal, Jr, *Chem. Phys. Lett.* **327**, 181 (2000).
- [80] J. Even, L. Pedesseau, J.-M. Jancu, and C. Katan, *J. Phys. Chem. Lett.* **4**, 2999 (2013).
- [81] J. Paier, R. Asahi, A. Nagoya, and G. Kresse, *Phys. Rev. B* **79**, 115126 (2009).
- [82] J. H. Skone, M. Govoni, and G. Galli, *Phys. Rev. B* **93**, 235106 (2016).

Supporting Material

Tunable Semiconductors: Control over Carrier States and Excitations in Layered Hybrid Organic-Inorganic Perovskites

Chi Liu,¹ William Huhn,² Ke-Zhao Du,² Alvaro Vazquez-Mayagoitia,³ David Dirkes,⁴ Wei You,⁴ Yosuke Kanai,⁴ David B. Mitzi,^{2,1} and Volker Blum^{2,1}

¹*Department of Chemistry, Duke University,
Durham, North Carolina 27708, USA*

²*Department of Mechanical Engineering and Materials Science,
Duke University, Durham, North Carolina 27708, USA*

³*Argonne Leadership Computing Facility,
9700 S. Cass Avenue, Lemont IL 60439, USA*

⁴*Department of Chemistry, University of North Carolina,
Chapel Hill, North Carolina 27599, USA*

(Dated: March 9, 2024)

SHORT DESCRIPTION

This Supplemental Material includes: structural details of the perovskites in our simulations; energetic impact of the supercell choice; impact of spin-orbit coupling in the reported energy band structures; computational details (basis sets and k-space grid convergence); validation of computational protocols by comparing to experimental results for MAPbI₃, for AE4TPbBr₄ and for AE4TPbI₄; experimental details for the synthesis and characterization of a new AE4TPbI₄ crystal; and additional computed orbitals, energy band structures, band curvature parameters, full and partial densities of states supporting the general findings demonstrated in the actual paper. Computational validation for MAPbI₃ also includes comparison to a more sophisticated many-body dispersion treatment.[1] Synthesis details include Refs. [2–4]. All computational input and output files (raw data) are available at the NOMAD repository.[5]

I. (2×2) SUPERCELL OF AE4TPbBr_4

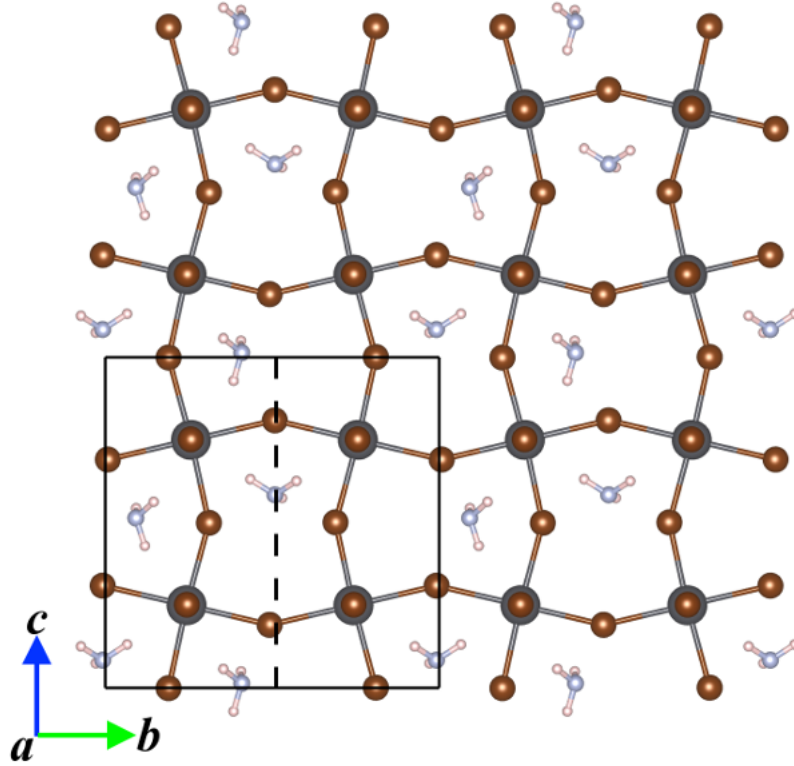


FIG. S1. Experimental structure of AE4TPbBr_4 viewed along the a -axis direction, adapted from Ref. [6]. Only the PbBr_4 framework and the NH_3 are shown for clarity. Two different configurations for the lead bromide framework and the ammonium tail can be seen arranged in an alternating fashion. Solid lines indicate the (2×2) cell in units of the hypothetical basic perovskite unit cell dimension, which is used as the basic structural unit in all calculations reported in the present work. The dashed line delineates the (1×2) unit cell model (which contained split atomic positions) as used in the X-ray refinement of AE4TPbBr_4 in Ref. [6].

II. COMPARISON OF (2×2) AND (1×2) STRUCTURE MODELS RELAXED BY DFT-PBE+TS

A. Nomenclature of Pb-X-Pb bond angles ($X = \text{Cl}, \text{Br}, \text{I}$)

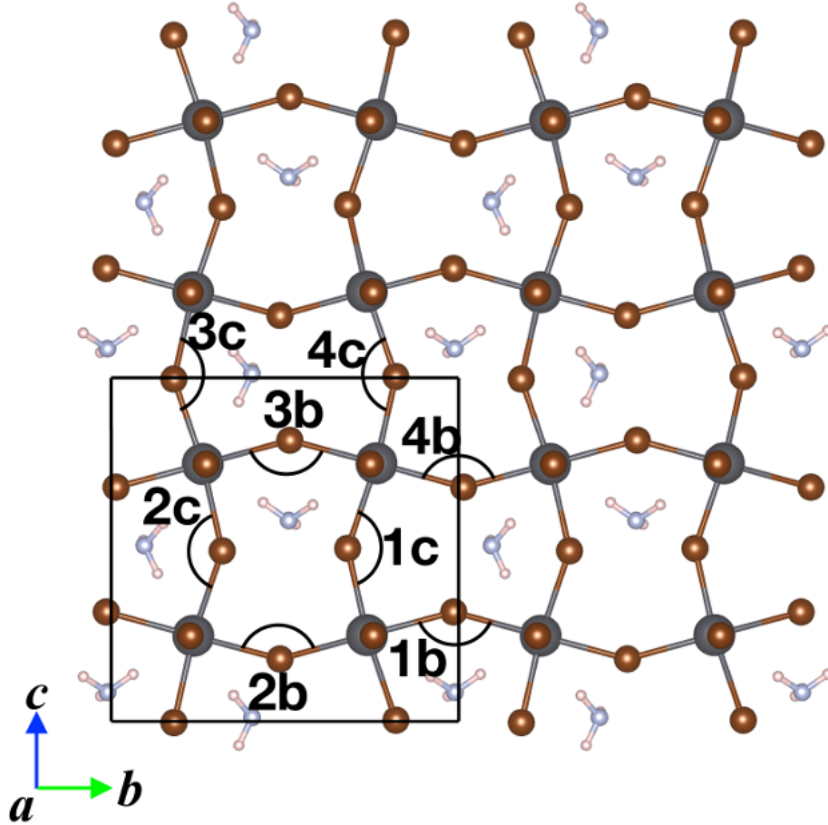


FIG. S2. Illustration of the Pb-X-Pb ($X = \text{Cl}, \text{Br}, \text{I}$) angles investigated in this paper for all hybrid compounds. The PBE+TS relaxed structure of AE4TPbX_4 is viewed from the a direction. Only the Pb-X inorganic framework and the NH_3 tails are shown for clarity. All other hybrid compounds discussed in this paper can be understood similarly. Two distinct inorganic PbX_4 layers are identified [e.g., see Fig. 1(a) in the main text] and labeled as layer 1 and layer 2. Each layer contains four PbX_4 octahedra (those inside the black solid line). There is one Pb-X-Pb angle along the b direction and one along the c direction for each PbX_4 octahedron. Therefore 8 distinct Pb-X-Pb angles exist for each inorganic layer, labeled as 1, 2, 3, 4 for b and c directions, respectively.

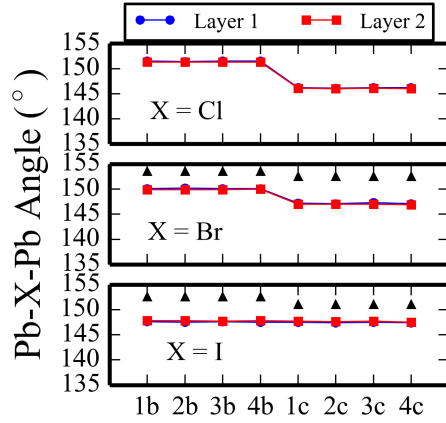


FIG. S3. Pb-X-Pb ($X = \text{Cl}, \text{Br}, \text{I}$) angles for AE4TPbX_4 ($X = \text{Cl}, \text{Br}, \text{I}$) HOIPs relaxed by DFT-PBE+TS using a (2×2) unit cell. The experimental angle values for AE4TPbBr_4 and AE4TPbI_4 are indicated by black triangles. No experimental data are available for the $X = \text{Cl}$ compound.

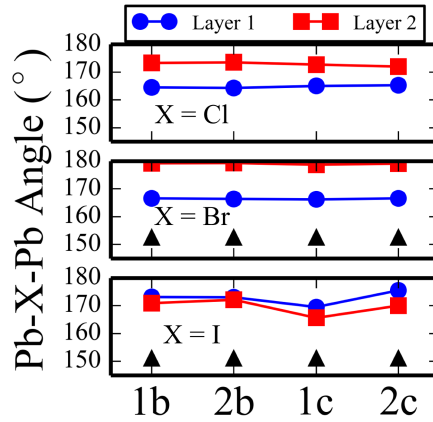


FIG. S4. Pb-X-Pb ($X = \text{Cl}, \text{Br}, \text{I}$) angles for AE4TPbX_4 ($X = \text{Cl}, \text{Br}, \text{I}$) HOIPs relaxed by DFT-PBE+TS using the (1×2) model unit cell. The experimental angle values for AE4TPbBr_4 and AE4TPbI_4 are indicated by black triangles.

B. PBE+TS total energy

TABLE S1. The PBE+TS total energy difference ($E(2\times 2) - E(1\times 2)$) of the PBE+TS predicted structure using the (1×2) and (2×2) unit cells for the syn-anti-syn $AE4TPbX_4$ ($X = \text{Cl, Br, I}$) and the all-anti $AEnTPbBr_4$ ($n = 2, 3, 4, 5$). K-point grids settings of $1\times 4\times 2$ were used for the (1×2) calculation, whereas $1\times 2\times 2$ k-point grids were used for the (2×2) calculation. The FHI-aims “tight” numerical defaults (Table S2) were used for both calculations. The total energy of the syn-anti-syn $AE4TPbBr_4$ is 2.44 eV/cell lower than that of the all-anti $AE4TPbBr_4$ compound (both in a (2×2) configuration).

Compounds	Energy Difference (eV)
$AE4TPbCl_4$	-2.49
$AE4TPbBr_4$	-2.70
$AE4TPbI_4$	-2.73
$AE2TPbBr_4$	-3.76
$AE3TPbBr_4$	-0.79
all-anti- $AE4TPbBr_4$	-1.50
$AE5TPbBr_4$	-0.83

III. EFFECT OF SPIN ORBIT COUPLING

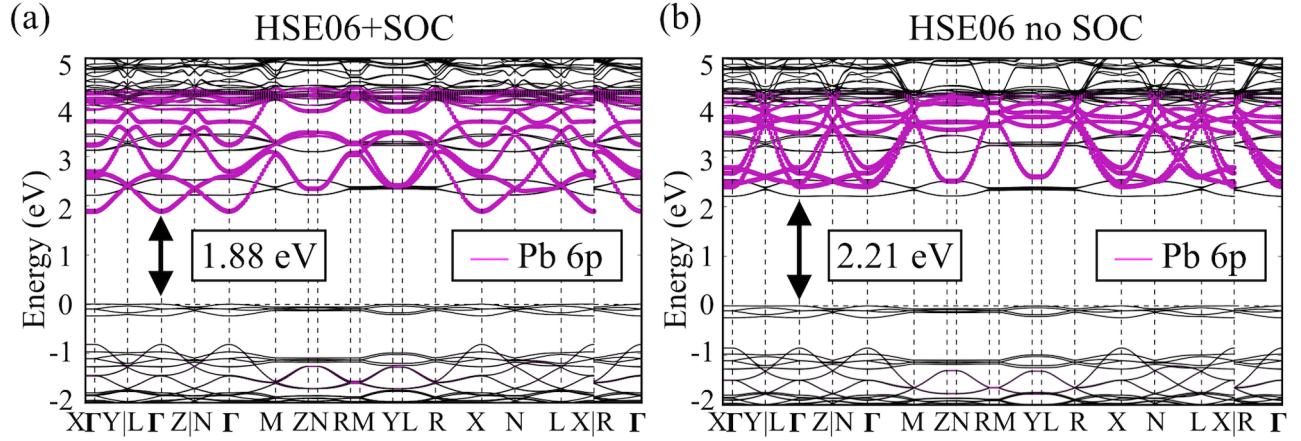


FIG. S5. (a) and (b) show the electronic band structures of AE4TPbBr₄ with the states of Pb-6p identified by Mulliken decompositions of the bands, calculated by DFT-HSE06+SOC and DFT-HSE06 without including SOC, respectively. The width of the colored lines is proportional to the Mulliken decomposition value of species or (in the case of Pb 6p) atomic orbitals of species they represent. Thus, wider colored lines correspond to bands having more contribution from the species or atomic orbitals of the species that the Mulliken decomposition is projected onto. The VBM and CBM are indicated by black arrows with the value of the band gap indicated.

IV. COMPUTATIONAL BASIS SETTINGS: TIGHT

TABLE S2. Basis functions (radial functions) in the “tight” computational settings used for the DFT-PBE+TS relaxation for H, C, N, O, S, Cl, Br, I and Pb elements.

	H	C	N	S
minimal	1s	[He]+2s2p	[He]+2s2p	[Ne]+3s3p
<i>tier 1</i>	H(2s,2.1) H(2p,3.5)	H(2p,1.7) H(3d,6.0) H(2s,4.9)	H(2p,1.8) H(3d,6.8) H(3s,5.8)	S ²⁺ (3d) H(2p,1.8) H(4f,7) S ²⁺ (3s)
<i>tier 2</i>	H(1s,0.85) H(2p,3.7) H(2s,1.2) H(3d,7.0)	H(4f,9.8) H(3p,5.2) H(3s,4.3) H(5g,14.4)	H(4f,10.8) H(3p,5.8) H(1s,0.8) H(5g,16) H(3d,6.2) H(3d,4.9)	H(4d,6.2) H(5g,10.8)
	Cl	Br	I	Pb
minimal	[Ne]+3s3p	[Ar]+4s4p3d	[Kr]+5s5p4d	[Xe]+6s6p5d4f
<i>tier 1</i>	Cl ²⁺ (3d) H(2p,1.9) H(4f,7.4) Cl ²⁺ (3s) H(5g,10.4)	H(3d,4.6) H(2p,1.7) H(4f,7.6) Br ²⁺ (4s)	H(3d,4) H(4f,6.4) H(2p,1.6) I ²⁺ (5s)	H(3p,2.3) H(4f,7.6) H(3d,3.5) H(5g,9.8) H(3s,3.2)
<i>tier 2</i>	H(3d,3.3)			

The first line (“minimal”) summarizes the free-atom radial functions used (noble-gas configuration of the core and quantum numbers of the additional valence radial functions). “H(nl, z)” denotes a hydrogen-like basis function for the bare Coulomb potential z/r , including its radial and angular momentum quantum numbers, n and l. $X^{2+}(nl)$ denotes a n, l radial function of a doubly positive free ion of species X. This nomenclature follows the convention employed in Table 1 of Ref. [7].

V. K-GRID CONVERGENCE TEST

TABLE S3. DFT-PBE total energy convergence with different k-grid settings for reciprocal-space integrals of AE4TPbBr₄.

K-grid	ΔE (eV)	ΔE (meV/atom)
1×2×2	0*	0*
2×4×4	-0.066	-0.16

* reference value

VI. COMPUTATIONAL BASIS SETTINGS: INTERMEDIATE

TABLE S4. Basis functions (radial functions) in the “intermediate” computational settings used for the DFT-HSE06+SOC calculation for H, C, N, O, S, Cl, Br, I and Pb elements.

	H	C	N	S
minimal	1s	[He]+2s2p	[He]+2s2p	[Ne]+3s3p
<i>tier 1</i>	H(2s,2.1)	H(2p,1.7)	H(2p,1.8)	S ²⁺ (3d)
	H(2p,3.5)	H(3d,6.0)	H(3d,6.8)	H(2p,1.8)
		H(2s,4.9)	H(3s,5.8)	H(4f,7)
				S ²⁺ (3s)
<i>tier 2</i>	H(1s,0.85)	H(4f,9.8)	H(4f,10.8)	H(5g,10.8) _{aux}
	H(3d,7.0) _{aux}	H(5g,14.4) _{aux}	H(5g,16) _{aux}	
	Cl	Br	I	Pb
Minimal	[Ne]+3s3p	[Ar]+4s4p3d	[Kr]+5s5p4d	[Xe]+6s6p5d4f
<i>tier 1</i>	Cl ²⁺ (3d)	H(3d,4.6)	H(3d,4)	H(3p,2.3)
	H(2p,1.9)	H(2p,1.7)	H(4f,6.4)	H(4f,7.6)
	H(4f,7.4)	H(4f,7.6)	H(2p,1.6)	H(3d,3.5)
	Cl ²⁺ (3s)	Br ²⁺ (4s)	I ²⁺ (5s)	H(5g,9.8) _{aux}
	H(5g,10.4)			H(3s,3.2)
<i>tier 2</i>	H(3d,3.3)			
		H(5g,10.8) _{aux}	H(5g,10.4) _{aux}	H(5g,9.4) _{aux}

The first line (“minimal”) summarizes the free-atom radial functions used (noble-gas configuration of the core and quantum numbers of the additional valence radial functions). “H(nl, z)” denotes a hydrogen-like basis function for the bare Coulomb potential z/r , including its radial and angular momentum quantum numbers, n and l . $X^{2+}(nl)$ denotes a n, l radial function of a doubly positive free ion of species X . This nomenclature follows the convention employed in Table 1 of Ref. [7]. The subscript “aux” denotes a basis function that is *not* used to expand the actual, generalized Kohn-Sham orbitals but that *is* used during the creation of the auxiliary basis sets that expand the screened Coulomb operator of the HSE06 functional, following the method described in Ref. [8].

VII. VALIDATION OF THE COMPUTATIONAL APPROACH

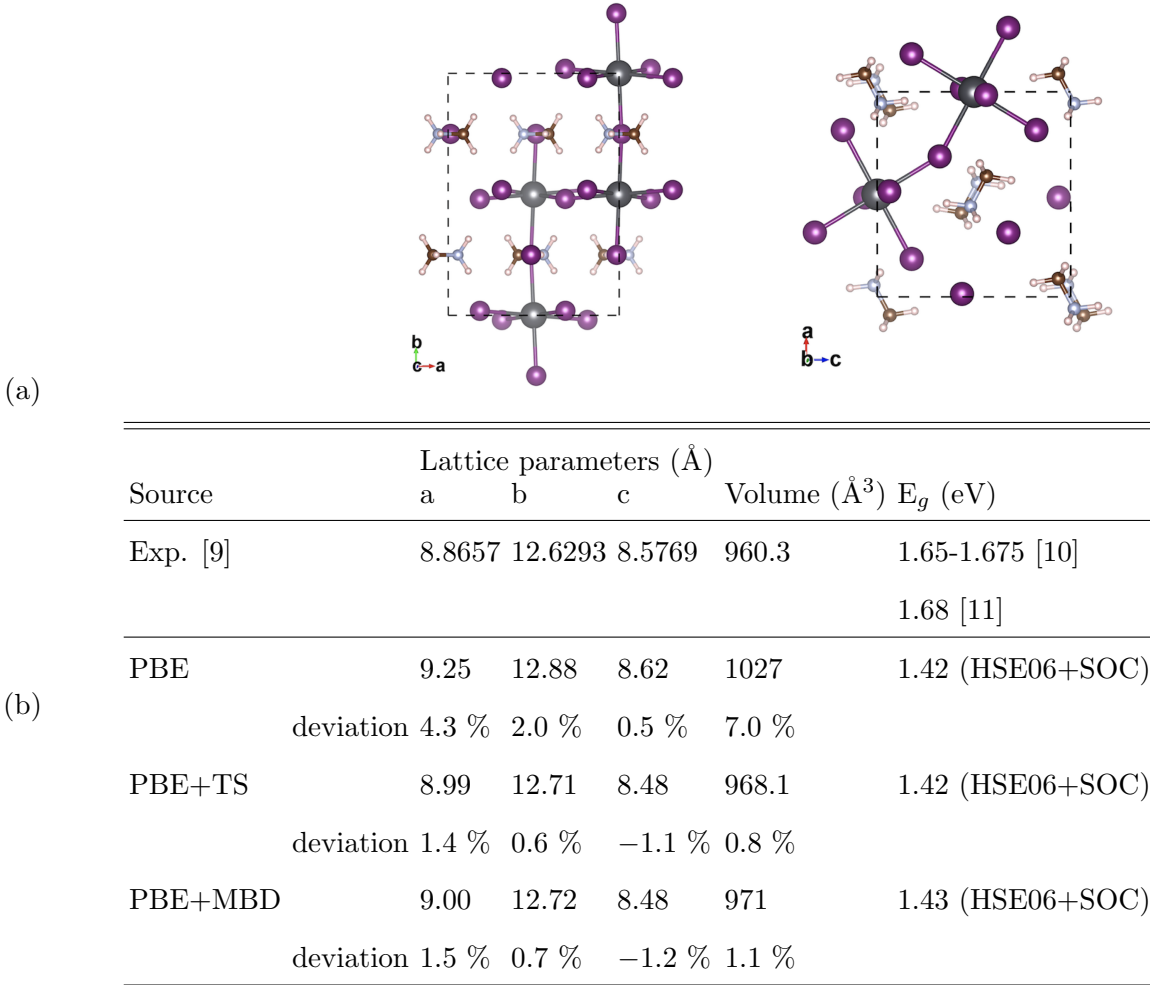


FIG. S6. (a) Structure of the low-temperature orthorhombic phase of MAPbI_3 from two different perspectives, fully relaxed by DFT-PBE+TS. (b) Lattice parameters and unit cell volume relaxed at different levels of DFT (PBE[12], PBE+TS[13] and PBE+MBD[1]), their deviation from experiment (neutron powder diffraction at $T=100$ K in Ref. [9]) and their impact on the predicted band gap by DFT-HSE06 including spin-orbit coupling (SOC) compared with the experimental value. The experimental band gap values shown reflect the apparent near-band-edge emission of orthorhombic MAPbI_3 observed at $T=10$ K by time-resolved photoluminescence in Ref. [10] and the optical transient absorption peak attributed to near-band-edge emission of orthorhombic MAPbI_3 at $T=15$ K in Ref. [11]. PBE+MBD stands for a more recent and more sophisticated many-body dispersion (MBD) scheme compared with PBE+TS to incorporate the vdW terms.[1] This comparison demonstrates that key parameters for MAPbI_3 remain unaffected by switching between the two different dispersion treatments.

VIII. OPTIMIZED STRUCTURES OF AE4TPbX₄ (X = Cl, Br, I)

TABLE S5. Computationally predicted unit cell parameters of AE4TPbX₄ (X = Cl, Br, I) relaxed by DFT-PBE+TS. The experimental structure refinements for AE4TPbBr₄[6] and AE4TPbI₄ (this work) are shown for comparison.

HOIPs	a(Å)	b(Å)	c(Å)	α	β	γ	V(Å ³)
AE4TPbCl ₄							
PBE+TS	40.85	11.29	10.95	90.0°	91.8°	90.0°	5049
AE4TPbBr ₄							
Exp.[6]	39.74	11.68	11.57	90.0°	92.4°	90.0°	5369
PBE+TS	40.01	11.60	11.47	90.0°	91.3°	90.0°	5322
Δ (%)	0.67	-0.74	-0.87	0.02	-1.17	0.04	-0.88
AE4TPbI ₄							
Exp.*	38.79	12.18	12.33	90.0°	92.3°	90.0°	5818
PBE+TS	39.02	12.10	12.22	90.0°	91.1°	90.0°	5771
Δ (%)	0.59	-0.65	-0.86	0.04	-1.31	0.04	-0.81

* see Section X, “Experimental details for AE4TPbI₄”, in this work.

IX. CONSTRUCTION OF THE COMPUTATIONAL STRUCTURE MODELS OF THE HOIP COMPOUNDS ASSESSED IN THIS WORK

We perform full relaxation of both unit cell parameters and cell-internal atomic coordinates on the initial input structure for all the HOIPs investigated. Initial models for the structure optimization were constructed as follows:

- **AE4TPbBr₄**: Taken as the experimental structure in Ref. [6].
- **AE4TPbX₄ (X = Cl, I)**: Obtained by taking the experimental structure of AE4TPbBr₄ and replacing the Br atoms with Cl and I. The lattice parameters and the atomic coordinates of non-halogen atoms were kept the same among the three hybrid compounds for the input structure. The initial configuration of AE4T molecules was kept to be syn-anti-syn as in the experimental structure of AE4TPbBr₄.
- **all-anti-AE4TPbBr₄**: Obtained by taking the experimental structure of AE4TPbBr₄ and changing the configuration of AE4T to all-anti. The inner two thiophene rings of the syn-anti-syn AE4T were rotated by 180° around the two C atoms labeled by red “+” as the rotation axis (Fig. S7). This rotation was performed for all the 8 AE4T molecules in the unit cell.

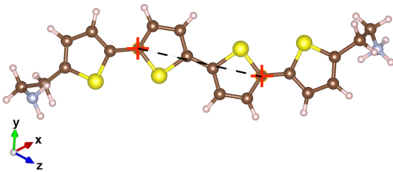


FIG. S7. Structure of the AE4T molecule in the experimental structure of AE4TPbBr₄ adopting the syn-anti-syn configuration.

- **AEnTPbBr₄ (n = 1, 2, 3, 5):** Obtained by taking the experimental structure of AE4TPbBr₄ and replacing the AE4T organic part by all-anti AEnT molecules. Using AE3T-PbBr₄ as an example, we start from the experimental structure of AE4TPbBr₄ with syn-anti-syn AE4T molecules. The oligothiophene part (4T) is removed while the inorganic Pb-Br framework together with the EtNH₃ tails are kept—i.e., the configuration of the Pb-Br framework together with the EtNH₃ tails is not changed during the construction. The adjacent inorganic layers are then pushed towards each other to reduce the distance between them to the extent that it is suitable for the insertion of the 3T molecules (all-anti). We then place the optimized 3T molecules into those positions where the 4T molecules originally existed (for AE4TPbBr₄). This construction process preserves the configuration between the inorganic Pb-Br framework and the EtNH₃ tails (Fig. S1) and keeps the two inorganic layers in each unit cell identical.

X. EXPERIMENTAL DETAILS FOR AE4TPbI₄

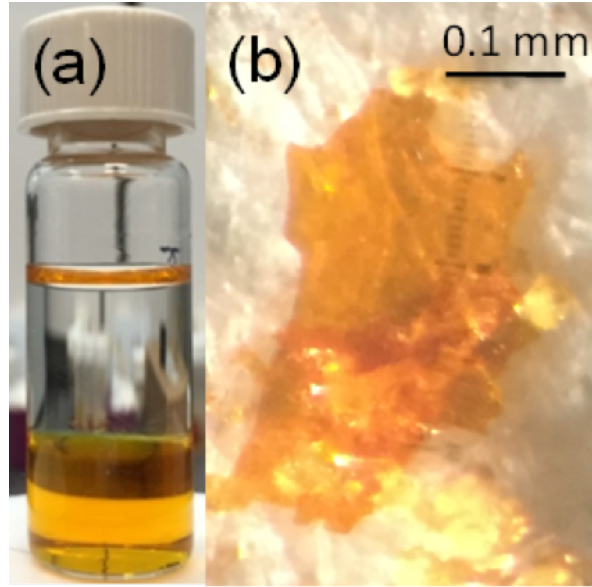


FIG. S8. Crystal of AE4TPbI₄

Chemical. PbI₂ (99.999% trace metal basis), HI (57 wt. % in H₂O, with hypophosphorous acid as stabilizer, assay 99.95%) and N,N-Dimethylformamide (anhydrous, 99.8%) were purchased from Sigma-Aldrich company. AE4T·HI was synthesized in the lab.[2–4] 2-butanol (99.5%) was purchased from VWR International.

Synthesis. 2 mg PbI₂ and 3 mg AE4T·HI were dissolved in 0.7 ml DMF with a drop of HI. Then, 2 ml 2-butanol was layered on the top of the solution (Figure S8a). The target crystals came out after several days (Figure S8b).

Characterization. Single crystal X-ray diffraction data were collected in a Bruker D8 ADVANCE Series II at room temperature. The unit cell parameters determined from this data are $a = 38.779(3) \text{ \AA}$, $b = 6.0863(5) \text{ \AA}$, $c = 12.3306(10) \text{ \AA}$, $\beta = 92.271(4)$, $V = 2908.0(4) \text{ \AA}^3$, C2/c.

XI. DFT-HSE06+SOC FRONTIER ORBITALS FOR AE4TPBX₄ (X=CL, BR, I)

	Real	Imag.	Real	Imag.	Real	Imag.	Real	Imag.
Spin Up								
Spin Down								
	Inorganic HOMO		Organic HOMO		Inorganic LUMO		Organic LUMO	
Energy (eV)	-1.20		0.00		2.12		2.18	
Mulliken Ratio (Org. / Inorg.)	0.08 / 0.92		1.00 / 0.00		0.01 / 0.99		0.99 / 0.01	

FIG. S9. Frontier orbitals of the organic and inorganic components of AE4TPbCl₄ at the Γ point, predicted by DFT-HSE06+SOC. The real and imaginary parts of the spin up and spin down channels of each spin-orbit coupled orbital are shown. Orbital energy values are given with respect to the overall HOMO energy as the energy zero. The Mulliken charge decomposition ratio of the organic component (C, H, N, S) over the inorganic component (Pb, Cl) is given. For each orbital type (organic/inorganic HOMO/LUMO), only one of two or more degenerate orbitals is shown. Individual orbitals can extend across equivalent parts of the structure in different ways since they can be linearly combined with their degenerate counterparts.

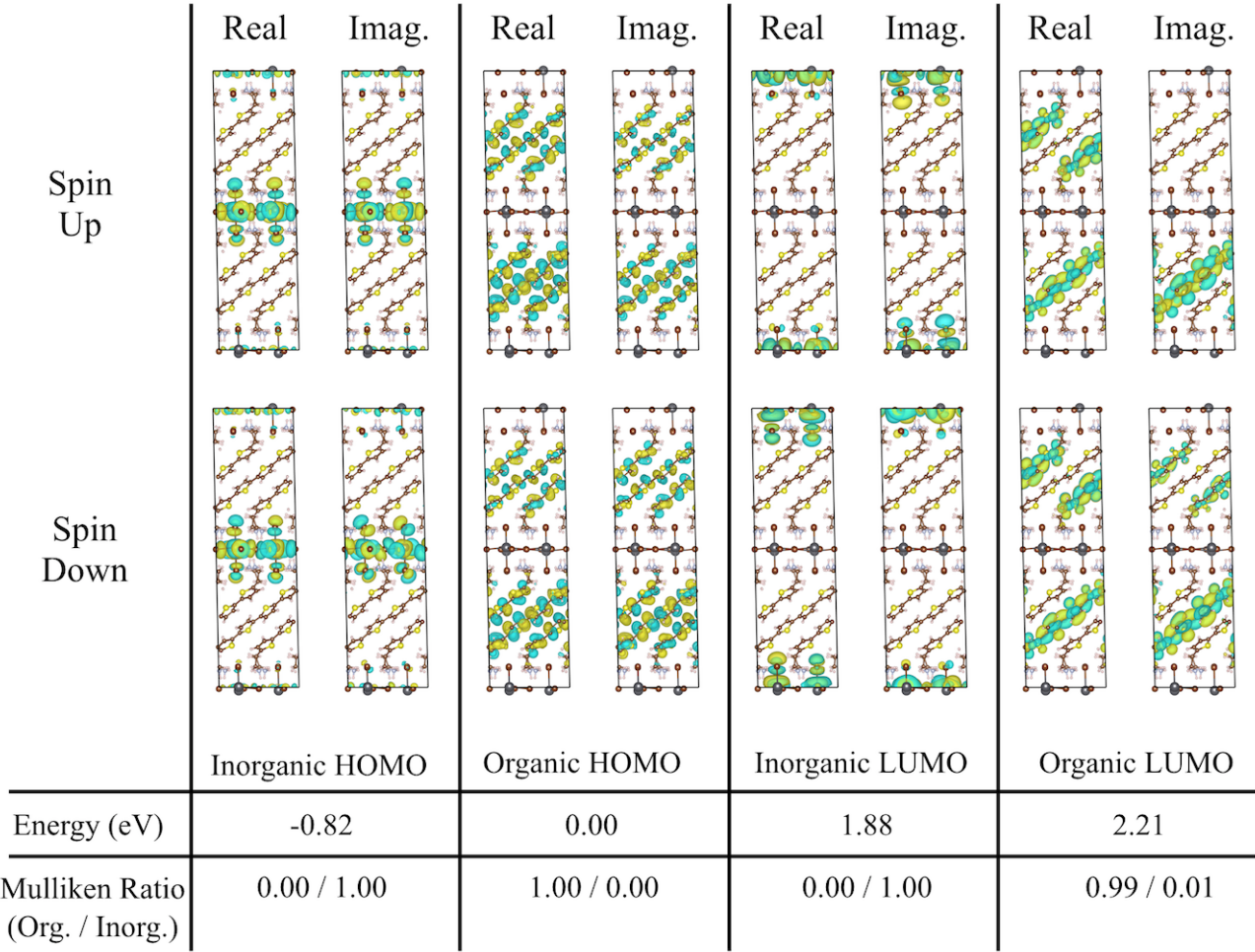


FIG. S10. Frontier orbitals of the organic and inorganic components of AE4TPbBr_4 at the Γ point, predicted by DFT-HSE06+SOC. The real and imaginary parts of the spin up and spin down channels of each spin-orbit coupled orbital are shown. Orbital energy values are given with respect to the overall HOMO energy as the energy zero. The Mulliken charge decomposition ratio of the organic component (C, H, N, S) over the inorganic component (Pb, Br) is given.

	Real	Imag.	Real	Imag.	Real	Imag.	Real	Imag.
Spin Up								
Spin Down								
	Inorganic HOMO		Organic HOMO		Inorganic LUMO		Organic LUMO	
Energy (eV)	-0.27		0.00		1.84		2.30	
Mulliken Ratio (Org. / Inorg.)	0.02 / 0.98		1.00 / 0.00		0.00 / 1.00		0.99 / 0.01	

FIG. S11. Frontier orbitals of the organic and inorganic components of AE4TPbI_4 at the Γ point, predicted by DFT-HSE06+SOC. The real and imaginary parts of the spin up and spin down channels of each spin-orbit coupled orbital are shown. Orbital energy values are given with respect to the overall HOMO energy as the energy zero. The Mulliken charge decomposition ratio of the organic component (C, H, N, S) over the inorganic component (Pb, I) is given. For each orbital type (organic/inorganic HOMO/LUMO), only one of two or more degenerate orbitals is shown. Individual orbitals can extend across equivalent parts of the structure in different ways since they can be linearly combined with their degenerate counterparts.

XII. DFT-HSE06+SOC BAND STRUCTURES OF $AEnTPbBr_4$ ($n = 1, 2, 3, 4, 5$)

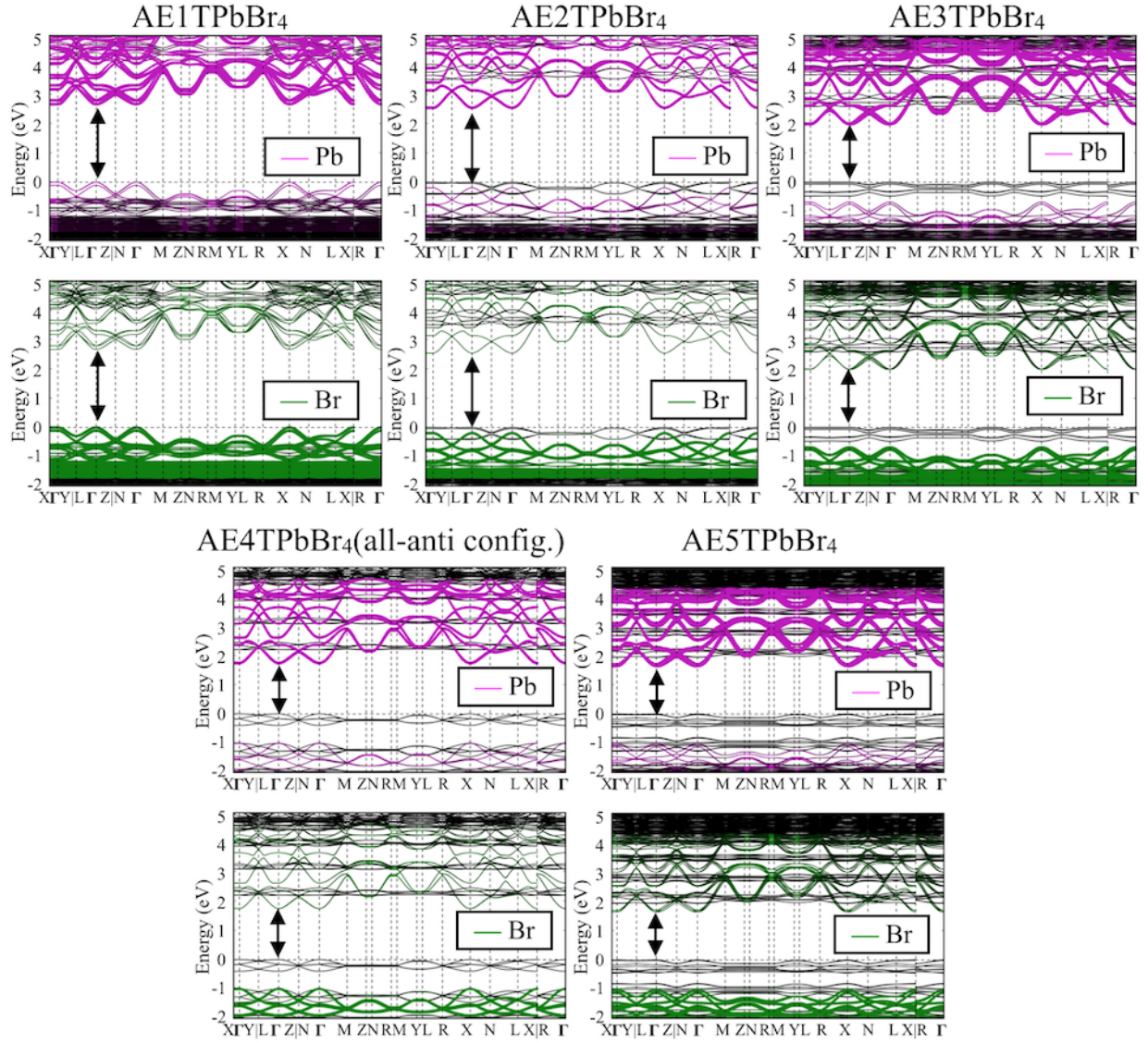


FIG. S12. Band structures of $AEnTPbBr_4$ ($n = 1, 2, 3, 4, 5$) with all-anti configuration of oligothiophene calculated by HSE06+SOC with the bands of Pb and Br (determined by Mulliken decompositions) colored on the band plot. The VBM and CBM are indicated by black arrows. For each orbital type (organic/inorganic HOMO/LUMO), only one of two or more degenerate orbitals is shown. Individual orbitals can extend across equivalent parts of the structure in different ways since they can be linearly combined with their degenerate counterparts.

XIII. HOMO-LUMO GAPS OF ISOLATED OLIGOTHIOPHENE MOLECULES

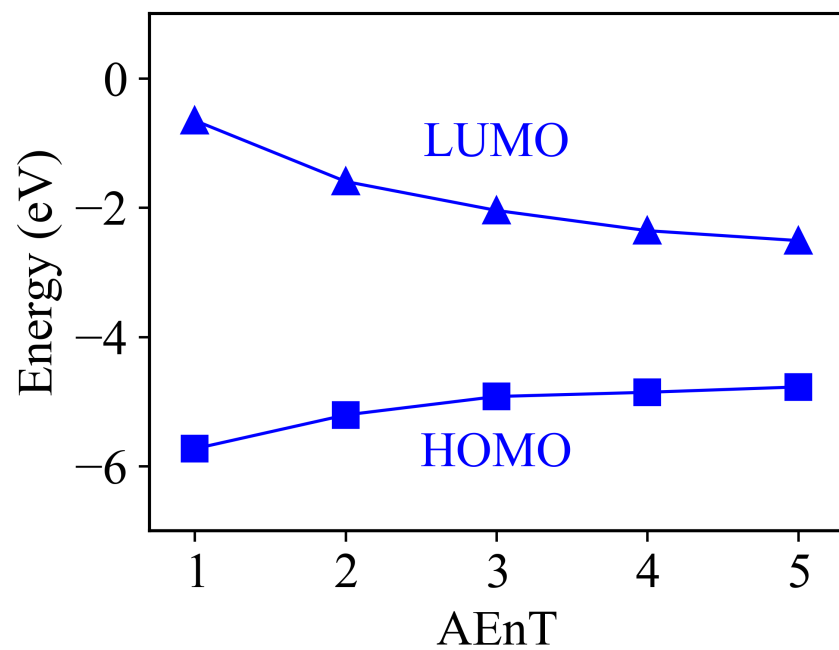


FIG. S13. Calculated HOMO and LUMO levels of the isolated oligothiophene molecules, $n=1-5$, with unprotonated $C_2H_5NH_2$ terminations.

XIV. EFFECTIVE MASS PARAMETERS DERIVED FROM THE BAND STRUCTURES COMPUTED IN THIS WORK

TABLE S6. Here and in Table S7, we provide anisotropic band curvatures (in effective mass units, m_e) at the Γ point, derived from the HSE06+SOC computed energy band structures for all compounds addressed in this work. For each material, separate band curvatures are given for the HOMO and the LUMO of the organic and the inorganic component. The absolute VBM and CBM of each material are marked with * symbols in the table. Corresponding band structure diagrams can be found in Figure 2 (main paper) and in Figure S12 of this supporting information. The curvature parameters were determined by parabolic fits to individual bands at the Γ points, in the directions parallel to the coordinate axes [see Figure 2(a) in the main paper], with small spacings of the fitted points of $0.01 a_0^{-1}$ or $0.02 a_0^{-1}$, where a_0 is the Bohr radius. The curvature parameters thus correspond to the diagonal elements of the effective mass tensor in this coordinate system, without a diagonalization of the effective mass tensor. Nevertheless, the diagonal elements give a clear qualitative indication of the band curvatures in the organic and inorganic components of each material considered. Large effective mass values correspond to essentially flat bands at the Γ point and are unlikely to be meaningful in the context of band-like transport; values above $20 m_e$ are therefore not further detailed in the table.

Material	Direction	HOMO (inorg.)	HOMO (org.)	LUMO (inorg.)	LUMO (org.)
AE4TPbCl ₄	Γ -X	>20	>20*	>20*	>20
	Γ -Y	0.42	>20*	0.32*	1.38
	Γ -Z	0.46	2.66*	0.43*	6.8
AE4TPbBr ₄	Γ -X	>20	>20*	>20*	>20
	Γ -Y	0.31	>20*	0.26*	1.57
	Γ -Z	0.33	2.23*	0.31*	15.9
AE4TPbI ₄	Γ -X	17.3	>20*	>20*	>20
	Γ -Y	0.27	>20*	0.22*	7.6
	Γ -Z	0.27	11.4*	0.22*	9.0

TABLE S7. Here and in Table S6, we provide anisotropic band curvatures (in effective mass units, m_e) at the Γ point, derived from the HSE06+SOC computed energy band structures for all compounds addressed in this work. See caption of Table S6 for details.

Material	Direction	HOMO (inorg.)	HOMO (org.)	LUMO (inorg.)	LUMO (org.)
AE1TPbBr ₄	Γ -X	11.1*	5.1	>20*	>20
	Γ -Y	0.37*	4.6	0.23*	0.97
	Γ -Z	0.38*	1.7	0.44*	1.08
AE2TPbBr ₄	Γ -X	>20	>20*	>20*	6.9
	Γ -Y	0.33	7.5*	0.23*	16.9
	Γ -Z	0.37	1.2*	0.36*	2.9
AE3TPbBr ₄	Γ -X	>20	>20*	>20*	>20
	Γ -Y	0.38	>20*	0.24*	2.8
	Γ -Z	0.39	1.9*	0.55*	>20
AE4TPbBr ₄ (all-anti)	Γ -X	16.3	>20*	>20*	>20
	Γ -Y	0.40	5.6*	0.24*	2.3
	Γ -Z	0.39	1.1*	0.35*	>20
AE5TPbBr ₄	Γ -X	>20	>20*	>20*	>20
	Γ -Y	0.55	7.3*	0.24*	5.5
	Γ -Z	0.54	1.2*	0.55*	2.8

XV. TOTAL AND PARTIAL DENSITIES OF STATES

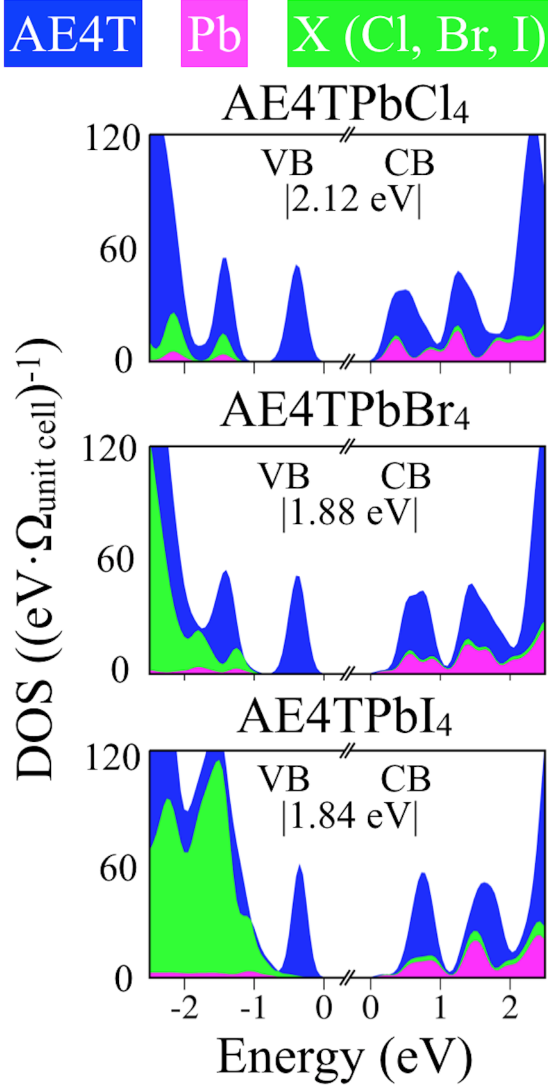


FIG. S14. Total densities of states (DOS) and element-projected DOS based on the DFT-HSE06+SOC for the HOIPs AE4TPbX₄ (X = Cl, Br, I). K-point grids settings of 3×3×3 were used in the DOS calculation. The Gaussian broadening parameter was 0.1 eV. The VBMs and CBMs are set to zero energy in each plot, with the actual band gap omitted. Band gap values are labeled in each subplot. The element-projected DOS is shown by different colors: magenta for Pb, green for halogens Cl, Br, I, and blue for organic component AE4T. The sum of all colored components is the total DOS, indicated by the outermost curve. Ω_{unit cell} in the Y axis label represents the volume of unit cell for each compound.

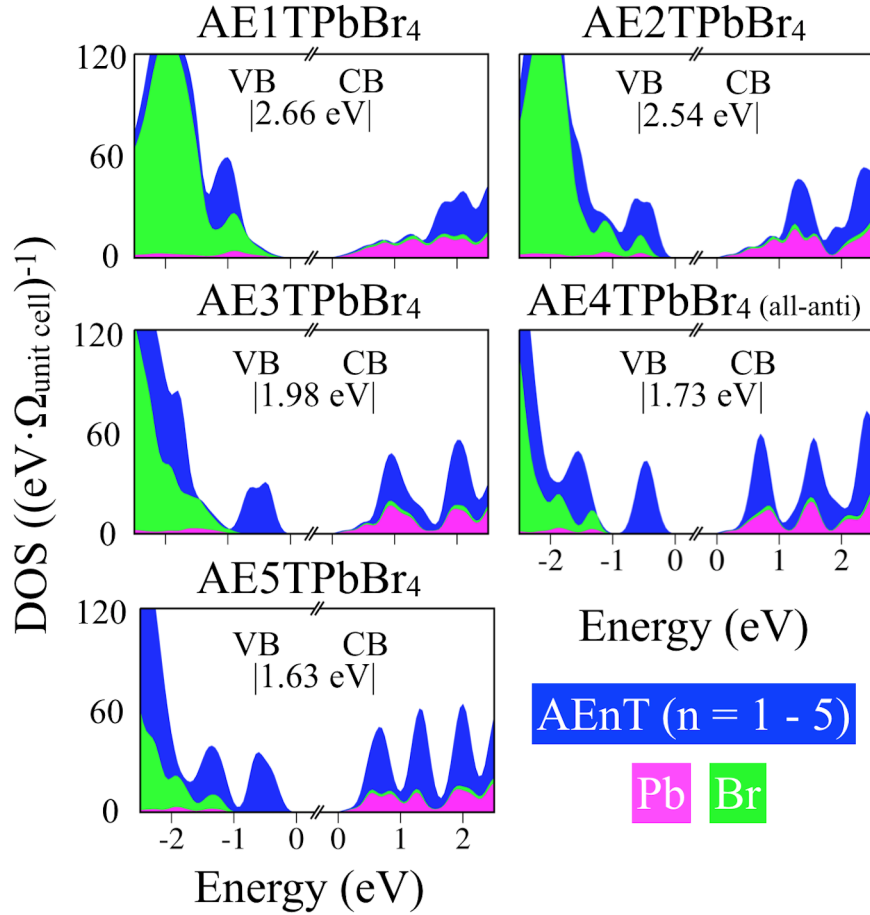


FIG. S15. Total densities of states (DOS) and element-projected DOS based on the DFT-HSE06+SOC for the HOIPs AEnTPbBr_4 ($n = 1, 2, 3, 4, 5$) with all-anti AEnT molecules. See caption of Fig. S14 for details.

-
- [1] A. Ambrosetti, A. M. Reilly, R. A. DiStasio Jr., and A. Tkatchenko, *J. Chem. Phys.* **140**, 18A508 (2014).
- [2] H. Muguruma, T. Saito, A. Hiratsuka, I. Karube, and S. Hotta, *Langmuir* **12**, 5451 (1996).
- [3] H. Muguruma, T. Saito, S. Sasaki, S. Hotta, and I. Karube, *J. Heterocyclic Chem.* **33**, 173 (1996).
- [4] H. Muguruma, K. Kobiro, and S. Hotta, *Chem. Mater.* **10**, 1459 (1998).
- [5] NOMAD Repository. <http://doi.org/10.17172/NOMAD/2018.09.21-1> (accessed Sep 22, 2018).
- [6] D. B. Mitzi, K. Chondroudis, and C. R. Kagan, *Inorg. Chem.* **38**, 6246 (1999).
- [7] V. Blum, R. Gehrke, F. Hanke, P. Havu, V. Havu, X. Ren, K. Reuter, and M. Scheffler, *Comput. Phys. Commun.* **180**, 2175 (2009).
- [8] A. C. Ihrig, J. Wieferink, I. Y. Zhang, M. Ropo, X. Ren, P. Rinke, M. Scheffler, and V. Blum, *New Journal of Physics* **17**, 093020 (2015).
- [9] M. T. Weller, O. J. Weber, P. F. Henry, A. M. Di Pumpo, and T. C. Hansen, *Chem. Commun.* **51**, 4180 (2015).
- [10] W. Kong, Z. Ye, Z. Qi, B. Zhang, M. Wang, A. Rahimi-Iman, and H. Wu, *Phys. Chem. Chem. Phys.* **17**, 16405 (2015).
- [11] L. Q. Phuong, Y. Yamada, M. Nagai, N. Maruyama, A. Wakamiya, and Y. Kanemitsu, *J. Phys. Chem. Lett.* **7**, 2316 (2016).
- [12] J. P. Perdew, K. Burke, and M. Ernzerhof, *Phys. Rev. Lett.* **77**, 3865 (1996).
- [13] A. Tkatchenko and M. Scheffler, *Phys. Rev. Lett.* **102**, 073005 (2009).